Ultramicroscopy 159 (2015) 67–72

Contents lists available at ScienceDirect

Ultramicroscopy

journal homepage: www.elsevier.com/locate/ultramic

Determination of the incommensurate modulated structure of $Bi_2Sr_{1.6}La_{0.4}CuO_{6+\delta}$ by aberration-corrected transmission electron microscopy

Binghui Ge [a,*], Yumei Wang [a], Huiqian Luo [a], Haihu Wen [a,1], Rong Yu [b], Zhiying Cheng [b], Jing Zhu [b]

[a] Beijing National Laboratory for Condensed Matter Physics, Institute of Physics, Chinese Academy of Sciences, Beijing 100190, China
[b] Beijing National Center for Electron Microscopy, Tsinghua University, Beijing 100084, China

ARTICLE INFO

Article history:
Received 18 March 2015
Received in revised form
3 August 2015
Accepted 23 August 2015
Available online 25 August 2015

Keywords:
Incommensurate modulated structure
Aberration-corrected transmission electron microscopy
Negative *Cs* imaging
Image deconvolution
High-dimensional space description

ABSTRACT

The incommensurate modulated structure (IMS) of $Bi_2Sr_{1.6}La_{0.4}CuO_{6+\delta}$ (BSLCO) has been studied by aberration-corrected transmission electron microscopy in combination with a high-dimensional (HD) space description. Two images are deconvoluted in the negative *Cs* imaging (NCSI) and positive *Cs* imaging (PCSI) modes. Similar results for the IMS have been obtained from two corresponding projected potential maps (PPMs), and the size of the dots representing atoms in the NCSI PPM is found to be smaller than that in the PCSI PPM. Considering that the object size is one of the factors that influence the precision of the structural determination, modulation functions for all unoverlapped atoms in BSLCO were determined on the basis of the NCSI PPM in combination with the HD space description.

1. Introduction

Incommensurate modulated structures (IMS) have been found to be strongly correlated with superconductivity in bismuth system cuprate superconductors [1]. In $Bi_{2+x}Sr_{2-x}CuO_{6+\delta}$, there exist displacive modulation and compositional modulation of Bi as shown by transmission electron microscope observation. Meanwhile, the distance between adjacent Bi-concentrated regions in the direction perpendicular to the modulation wave vector is found to be inversely proportional to the superconducting transition temperature (T_c), and the angle between the modulation wave vector and the $\boldsymbol{b}^*$ axis, [1]. Scanning tunneling microscope observations provide evidence that variations in the distance between the apical oxygen and the planar copper atoms within individual unit cells due to the IMS affect the superconducting energy-gap maximum of $Bi_2Sr_2CaCu_2O_{8+\delta}$ [2]. Although not all structural refinements support this conjecture, it is still an important step in understanding the dependence of T_c on the crystal structure [3]. In reality, however, the accurate crystal structure of IMS in cuprate superconductors is an object of contention even after 20 years of study because of its complexity.

High-resolution transmission electron microscopy (HRTEM) is a powerful method for structural determination, especially for minute crystals or crystals with weak structural signals, such as modulation structures. However, due to the existence of objective lens aberrations a random high-resolution (HR) image may not reflect the real structure. Even at the Scherzer focus condition [4], the point resolution of conventional medium-voltage electron microscopes is limited to approximately 0.2 nm such that not all atoms can be resolved. Posterior image processing methods such as exit-wave reconstruction [5–10] and electron-crystallography image processing [10–18] are usually used to correct the image distortion and extract the HR information. For the structural complexity of IMS, image deconvolution [13], one of electron-crystallography image processing methods, will be applied in this manuscript in combination with the Fourier filtering and high-dimensional spatial symmetry averaging.

Great progress has been made since aberration correctors were invented in the 1990s [19–22]. Point resolution has been enhanced even beyond the information limit and light atoms such as oxygens in oxides can be directly observed [23]. As the resolution of microscopes is enhanced to the subangstrom scale, however, image contrast becomes exceedingly sensitive to changes in imaging conditions [24–26]. Even at the Scherzer focus condition, artefacts may be introduced into images when the spherical aberration

* Corresponding author.
E-mail address: bhge@iphy.ac.cn (B. Ge).
[1] Present address: Department of Physics, Nanjing University, Nanjing 210093, China.

http://dx.doi.org/10.1016/j.ultramic.2015.08.004
0304-3991/

coefficient is corrected to close to 0. Therefore, image processing is still necessary for structural determination in aberration-corrected electron microscopy [24–27].

In this article, the method of image deconvolution [13] is applied to study the IMS in the optimally doped bismuth system cuprate superconductor $Bi_2Sr_{1.6}La_{0.4}CuO_{6+\delta}$ (BSLCO) by using aberration-corrected electron microscope. Similar IMSs in the superconductor oxides $Bi_2Sr_2CaCu_2O_x$ [28] and $(Pb_{0.5}Sr_{0.3}Cu_{0.2})Sr_2(Ca_{0.6}Sr_{0.4})_2Cu_3O_y$ [29] were studied in the 1990s. Structural information with a resolution of approximately 1 Å was obtained by combining image deconvolution with electron diffraction data, but due to the complexity of the IMS, the quantitative structural information of in these two compounds is still an open question. In this article, two HR images taken with different imaging mode of aberration-corrected TEM, positive *Cs* imaging (PCSI) and negative *Cs* imaging (NCSI) [23,30–33] are analyzed and compared. The size of the dots representing atoms in the NCSI projected potential map (PPM) is found to be smaller than that in the PCSI PPM, which makes the NCSI more quantitative for structural determination. From the results of the NCSI, the modulation functions of all unoverlapped atoms, including Cu and O in the CuO planes, are determined with the help of the high-dimensional (HD) space description [34].

2. HD space description

Due to absence of three-dimensional translation symmetry, the IMS cannot be described by three-dimensional crystallography, so the HD space description [34] should be taken into consideration during the structural determination of the IMS, and will be introduced briefly in the following.

In IMS, there are two types of reflections in the reciprocal space. The stronger one, known as the main reflection, reflects the information of the average structure; while the weaker one, known as the satellite reflection, carries the modulated information. To index all reflections, an extra modulation wave vector $\boldsymbol{q}$ should be introduced. Here a one-dimensional (1D) IMS is taken as an example, where the reciprocal lattice vectors are expressed as follows:

$$\boldsymbol{H} = h\boldsymbol{a}^* + k\boldsymbol{b}^* + l\boldsymbol{c}^* + m\boldsymbol{q}, \quad (1)$$

where h, k, l and m are integers, and $\boldsymbol{a}^*$, $\boldsymbol{b}^*$ and $\boldsymbol{c}^*$ are the reciprocal basis vectors, and the modulation wave vector is expressed as $\boldsymbol{q}=\alpha\boldsymbol{a}^*+\beta\boldsymbol{b}^*+\gamma\boldsymbol{c}^*$ where at least one of α, β and γ is irrational.

A vector $\boldsymbol{e}$ perpendicular to the space ($\boldsymbol{a}$, $\boldsymbol{b}$, $\boldsymbol{c}$) is introduced to construct a four-dimensional (4D) periodic structure ($\boldsymbol{a}-\alpha\boldsymbol{e}$, $\boldsymbol{b}-\beta\boldsymbol{e}$, $\boldsymbol{c}-\gamma\boldsymbol{e}$, $\boldsymbol{e}$) for a 1D IMS, where the atoms are 1D and periodic along the fourth axis $\boldsymbol{e}$ and different shapes represent different types of modulations. For instance, atoms look like wavy strings of uniform thickness in displacive modulations and like straight strings with a fluctuating thickness in occupational modulations.

3. Experimental procedure

Single crystal BSLCO samples of high quality are prepared from mixed powders of Bi_2O_3, $SrCO_3$, La_2O_3 and CuO with nominal compositions by the traveling-solvent floating-zone technique. The post-annealing experiment is carried out in flowing oxygen at high temperature [35]. The [100] specimen for the electron microscope observation is prepared by cutting, mechanical polishing and ion milling, as described in Ref. [1]. The specimen is observed by means of a Titan 80–300 electron microscope with the information limit of approximately 0.8 Å. The image processing such as the superspace symmetry averaging and image deconvolution are performed by using VEC [36], and the modulation functions are determined by the method described in Ref. [37].

4. Results and discussion

4.1. Determination of the PPM of the IMS

As in its mother system $Bi_2Sr_2CuO_{6+\delta}$ [1], there exists a 1D IMS in the $\boldsymbol{bc}$ plane of BSLCO. The modulated wave vector is determined from its [100] projected electron diffraction pattern to be $\boldsymbol{q}$=0. 24$\boldsymbol{b}$*+$\boldsymbol{c}$* as shown in Fig. 1 where $\boldsymbol{b}$* and $\boldsymbol{c}$* are the reciprocal basis vectors of BSLCO, and its superspace group is $Bbmb(0\beta1)$. Fig. 2(a) is a corresponding HR image with residual aberrations of *Cs* equal to 0.05 mm and *C*1 -11 nm. After Fourier filtering to reduce the random noise in the selected circular area, HD symmetry averaging is carried out with the superspace group $Bbmb(0\beta1)$ to correct the influence of crystal tilt and/or beam tilt, and also correct residual Azimuth-dependent aberrations to some extent, such as astigmatism and coma. For the image is taken near the Scherzer focus, two adjacent large black dots in the symmetry-averaged image (see Fig. 3(a)) represent Bi(O) atomic columns according to the basic structural model of $Bi_2Sr_2CuO_6$ (BSCO) as shown in Fig. 3 (b) [38], and the small black dots represent Sr(La, O) columns. Changes in contrast and atomic positions in the Bi(O) and Sr(La, O) layers confirm the existence of both compositional and displacive modulations. Due to the residual aberrations the Cu and O columns in the CuO plane are not resolved.

To correct the image distortion caused by the contrast transfer function trial deconvolution is carried out using defocus values in the range of −5 nm to −20 nm with an interval of 1 nm, and the most likely value is determined to be −13 nm according to the basic structural model of BSCO (see Fig. 3(b)). In the deconvoluted image shown in Fig. 3(c), which represents the projected potential of the IMS and hence is called the PPM, the Cu and O atoms in the CuO plane have been resolved, and displacive modulations waves at Cu and O positions can be observed.

In addition to the PCSI mode with a negative focus value, the NCSI [23,30–33] mode with a positive focus value has been widely applied to investigate light atoms, such as the oxygens in oxides, due to its enhanced image contrast, which is thought to originate from the constructive superposition of the linear and non-linear contribution to the total image contrast [31]. In this work, NCSI is also utilized to study the IMS in BSLCO, and the two imaging modes are compared using experimental and simulated images.

Fig. 2(b) is the experimental HR image of BSLCO with *Cs* of approximately −0.013 mm and *C*1 4 nm (near the Scherzer focus

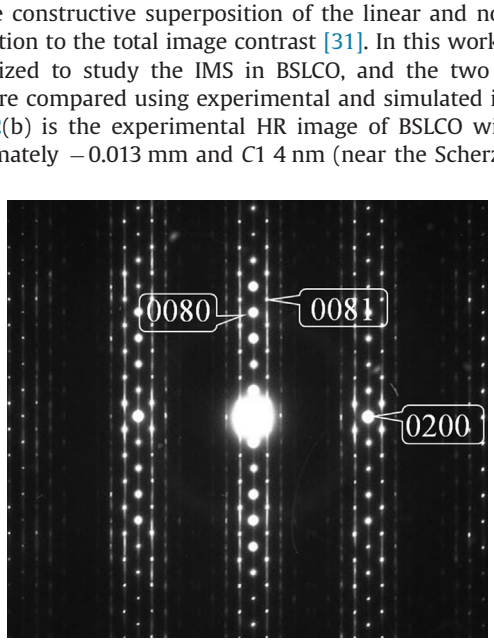

Fig. 1. [100] electron diffraction pattern.

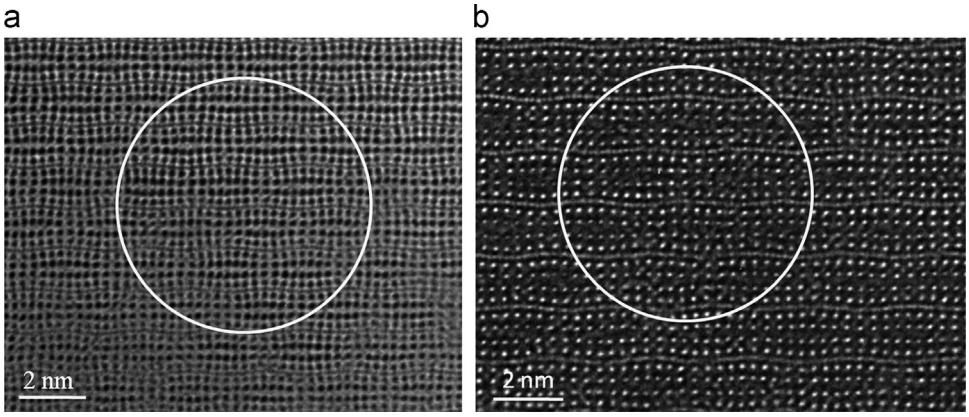

Fig. 2. (a) and (b) [100] HR images of BSLCO with $Cs=0.05$ and -0.013 mm, respectively. The circular area is selected for further image processing.

condition). Fourier filtering, HD symmetry averaging and image deconvolution are carried out as mentioned above, and the symmetry-averaged image and deconvoluted one with the defocus value 4 nm are shown in Fig. 4(a) and (b), respectively. The same results for the IMS can be obtained from Fig. 4(b) as from Fig. 3 (c) that there are strongly displacive modulations in the Bi(O), Sr (La, O) and CuO layers and clear compositional modulations in the Bi(O), and Sr(La, O) layers. The image contrast at the Bi position is found to be abnormally weaker than that at the Sr position in Fig. 4(b) despite the larger atomic number of Bi, which can be explained based on the effect of the crystal thickness on the image contrast variation that is predicted by the theory of the pseudo-weak-phase object approximation [39].

By comparing two PPMs in different imaging modes, a clear difference can be observed that the size of the dots for heavy atoms in Fig. 3(c) (PCSI) is much larger than that in Fig. 4(b) (NCSI) such as the Bi(O) and Sr(La, O) columns. To interpret this phenomenon, a multislice simulation was carried out based on the basic structural model of BSCO.

Fig. 5(a) and (b) are thickness-series simulated images in the NCSI mode ($Cs=-0.013$ mm) and PCSI mode ($Cs=0.013$ mm), respectively, with corresponding corrected Scherzer focus conditions [40,41]. Both of them can be regarded as structural images, but the difference is that in Fig. 5(a) (NCSI mode) white dots represent atoms while in Fig. 5(b) (PCSI mode), the atoms are black dots. As in the results obtained from the experimental images, the size of the dots in NCSI is smaller than that in PCSI for the heavy atoms Bi(O) and Sr(O). Moreover, with the increase of the sample thickness the size of the dots decreases for NCSI mode, while it increases for PCSI mode. As reported in Ref. [42], object size is one important factors that influences the precision of the atomic position determination besides the atomic distance, resolution of the instrument and the number of electron counts, so NCSI mode is more suitable for quantitative structural determination. In the following, the PPM obtained from the NCSI image (Fig. 4(b)) will be used to determine the modulation functions of the IMS of BSLCO with the help of the HD space description. Further results about the size of the dots in the structural images are given in the Ref. [43].

4.2. Determination of modulated functions

As mentioned in Section 2, atoms for the 1D IMS can be treated as 1D and periodic strings along the fourth axis in 4D space, so to quantitively determinate the IMS, modulation functions should be determined to describe the fluctuations of the string, which in fact are deviations of the atomic position and occupation from the averaged values. The method suggested by Ref. [37] to determine the modulated functions using only the limited-size PPM, like Fig. 4(b) will be introduced briefly.

In the case of BSLCO, the modulation vector lies in the (***b***, ***c***) plane, so there is a discrepancy between the IMS and the average structure (only the main reflection is included) in the atomic position and atomic occupancy in the ***y*** and ***z*** directions. A series of deviations in the atomic position denoted by Δy and Δz, and in the atomic occupancy denoted by Δp, can be obtained for a certain symmetry-independent atom in different unit cells by comparing the PPMs of the average structure and the IMS. According to the

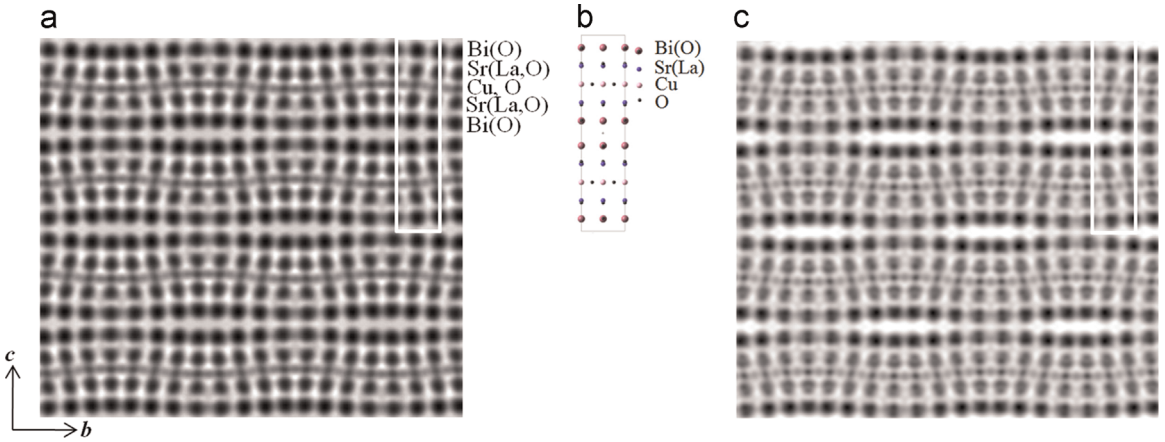

Fig. 3. (a) Symmetry-averaged image of IMS corresponding to the circular area in Fig. 2(a) and (b) basic structural model of BSCO, and (c) deconvoluted image of (a) with $Cs=0.05$ mm and defocus value $C1\ -13$ nm. A white rectangle is used to indicate the unit cell.

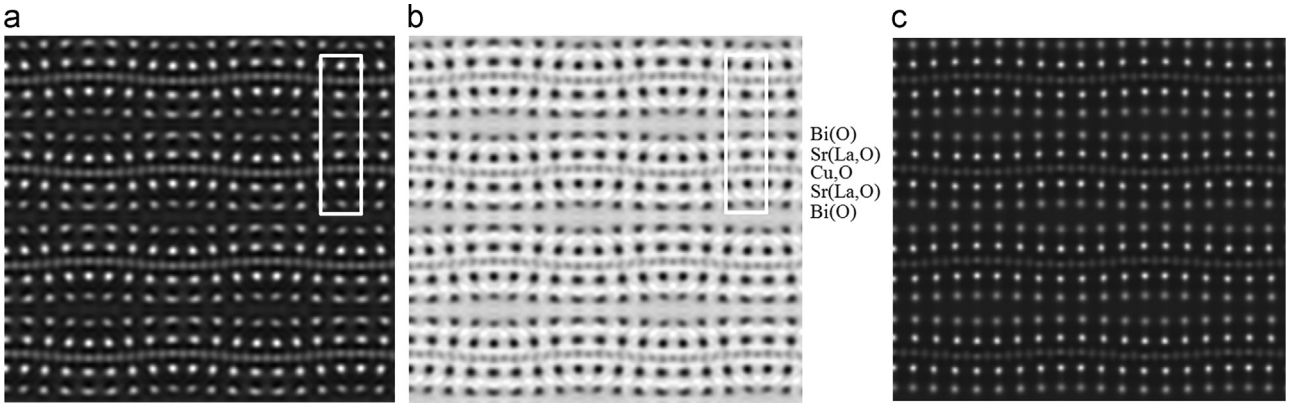

Fig. 4. (a) and (b) Symmetry-averaged and deconvoluted images of BSLCO corresponding to the circular area in Fig. 2(b), respectively. (c) Simulated image based on the modulation functions with parameters shown in Table 1. A white rectangle is used to indicate the unit cell.

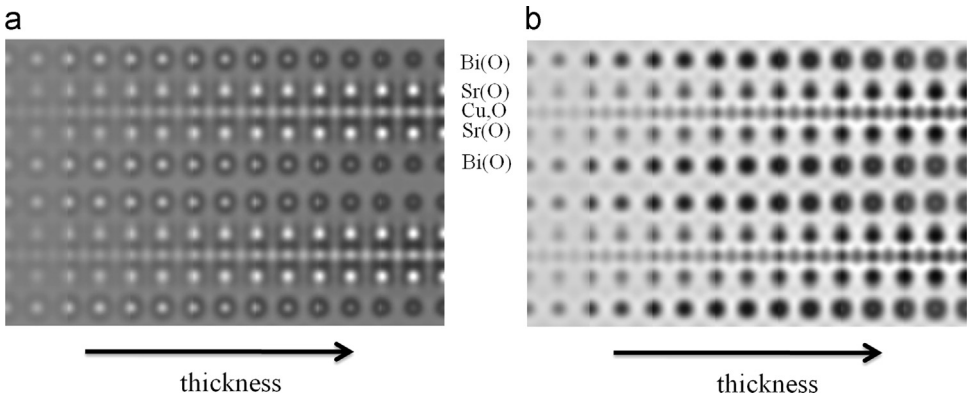

Fig. 5. (a) and (b) Simulated image based on the basic structural model of BSCO in NCSI mode (*Cs* −0.013 mm) and PCSI mode (*Cs* 0.013 mm), respectively. In (a) bright dots represent atoms while in (b), atoms are black dots. Thickness for simulation increases from left (0.5 nm) to right (3.8 nm) with an interval of 0.55 nm.

Table 1
Parameters of modulation functions of the IMS in BSLCO obtained from the [100] PPM shown in Fig. 4(b) and used to simulate the image shown in Fig. 4(c).

Symmetry independent atoms	Average position and average occupancy		Parameters of modulated function				
			Deviations in atomic position and occupancy	Coefficient (j=1,2)			
				A_1	B_1	A_2	B_2
Bi	$\bar{y}$	−0.0015	Δy	0.0235	−0.0512	−0.0035	0.0015
	$\bar{z}$	0.0642	Δz	0.0047	0.0074	−0.0036	−0.0004
	$\bar{p}$	1.0000	Δp	−0.0994	−0.0517	−0.0398	−0.0153
Sr	$\bar{y}$	0.0008	Δy	0.0314	−0.0163	−0.0044	−0.0017
	$\bar{z}$	0.1714	Δz	0.0047	0.0083	0.0000	−0.0001
	$\bar{p}$	0.8000	Δp	0.0604	0.0414	−0.0029	0.0161
La	$\bar{y}$	0.0008	Δy	0.0314	−0.0163	−0.0044	−0.0017
	$\bar{z}$	0.1714	Δz	0.0047	0.0083	0.0000	−0.0001
	$\bar{p}$	0.2000	Δp	0.0604	0.0414	−0.0029	0.0161
Cu	$\bar{y}$	0.0000	Δy	−0.0052	0.0025	−0.0024	0.0038
	$\bar{z}$	0.2500	Δz	−0.0025	0.0144	−0.0011	0.0003
	$\bar{p}$	1.0000	Δp	0	0	0	0
O	$\bar{y}$	0.2531	Δy	−0.0028	0.0050	0.0019	0.0083
	$\bar{z}$	0.2499	Δz	0.0006	0.0100	−0.0001	0.0004
	$\bar{p}$	1.0000	Δp	0	0	0	0

$\bar{y}$ and $\bar{z}$ are the average coordinates in the ***b*** and ***c*** direction, respectively, $\bar{p}$ is the average occupancy. Δz, Δy and Δp are their corresponding deviations. Deviations are expressed in the form of the Fourier series $\Delta f(t)=\sum_{j=1}^{2}[A_j\cos(2\pi t^*j)+B_j\sin(2\pi t^*j)]$.

HD space description [34], the deviation can be parameterized with the averaged 4D coordinate t, which can be determined from the equation

$$t = \boldsymbol{q}\cdot\bar{\boldsymbol{r}}, \quad (2)$$

where $\boldsymbol{q}$ is the modulation vector, and $\bar{\boldsymbol{r}}$ is the coordinate of an atom in a different unit cell in the image of the average structure. After a series of mathematical processing on $\Delta y(t)$, $\Delta z(t)$ and $\Delta p(t)$, the coefficients of the modulation functions A_j and B_j can be

derived from the formula.

$$\Delta f(t) = \sum_{j=1}^{n} \left[A_j \cos(2\pi t^* j) + B_j \sin(2\pi t^* j) \right], \quad (3)$$

where $f = y, z, p$. Because the coefficients A_j and B_j steeply decrease with the increase of the order j in BSLCO, only the first two terms are meaningful.

Based on this method, the modulation functions for all unoverlapped symmetry-independent atoms in BSLCO have been determined with the parameters listed in Table 1. Because the image contrast is affected by the background subtraction and intensity scaling, it is hard to precisely measure the occupancy of the atoms so that the relative deviation of the occupancy is more concerned here. Hence, the average occupancy in the Bi position by Bi atoms is set to be 1 although there should be a mixture of Bi and Sr(La) atoms when we consider that there exist compositional modulations in the Bi layer, similar to in the Sr(La) positions. Moreover, occupational modulations in the Cu and O sites are neglected for their small atomic numbers and consequently large errors. HD multislice simulation [44] is carried out with the parameters of the modulated functions shown in Table 1. The simulated image shown in Fig. 4(c) matches Fig. 4(a) very well with $Cs = -0.013$ mm and defocus value 4 nm, which verifies the validity of the modulated functions.

5. Conclusions

The IMS of BSLCO has been studied by means of aberration-corrected electron microscopy in combination with HD space description. The PPM of the IMS is obtained with all unoverlapped atoms resolved after image deconvolution, and the displacive modulations in the Bi(O), Sr(La, O) and CuO layers are found as well as the occupational modulations in the Bi(O) and Sr(La, O) layers.

By comparing the PPMs obtained from the images in two different imaging modes, the size of the dots in NCSI PPM is found to be smaller than that in the PCSI PPM, especially for heavy atoms, which is evidenced by image simulation. Because the size of the dots influences the precision of the atomic position determination, the NCSI PPM is used to determine the modulation functions of all unoverlapped atoms with the help of the HD space description. Validation of the functions is performed by HD multislice simulation.

Acknowledgments

This work was supported by the National Basic Research Program of China (Grant number: 2011CBA001001) and the National Natural Science Foundation of China (Grant number: 11104327, 11374332, 11474329). This work made use of the resources of the Beijing National Center for Electron Microscopy at Tsinghua University.

References

[1] X.M. Li, F.H. Li, H.Q. Luo, L. Fang, H.H. Wen, Transmission electron microscopy study of one-dimensional incommensurate structural modulation in superconducting oxides BSCO, Supercond. Sci. Technol. 22 (2009) 065003.
[2] J.A. Slezak, J. Lee, M. Wang, K. McElroy, K. Fujita, B.M. Andersen, P.J. Hirschfeld, H. Eisaki, S. Uchida, J.C. Davis, Imaging the impact on cuprate superconductivity of varying the interatomic distances within individual crystal unit cells, Proc. Natl. Acad. Sci. USA 105 (2008) 3203–3208.
[3] M.R. Norman, Modulated pairs in superconducting cuprates, Proc. Natl. Acad. Sci. USA 105 (2008) 3173–3174.
[4] O. Scherzer, The theoretical resolution limit of the electron microscope, J. Appl. Phys. 20 (1949) 20–29.
[5] P. Schiske, Zur Frage der Bildrekonstruktion durch Fokusreihen, in: Proceedings of the 4th European Conference on Electron Microscopy, Rome, 1968, pp. 145–146.
[6] W.O. Saxton, Computer Techniques for Image Processing in Electron Microscopy, Academic Press, New York, San Francisco, London, 1978.
[7] E.J. Kirkland, Improved high-resolution image-processing of bright field electron-micrographs. I. Theory, Ultramicroscopy 15 (1984) 151–172.
[8] E.J. Kirkland, B.M. Siegel, N. Uyeda, Y. Fujiyoshi, Improved high-resolution image-processing of bright field electron-micrographs. II. Experiment, Ultramicroscopy 17 (1985) 87–103.
[9] W.M.J. Coene, A. Thust, M. Op de Beeck, D. Van Dyck, Maximum-likelihood method for focus-variation image reconstruction in high resolution transmission electron microscopy, Ultramicroscopy 64 (1996) 109–135.
[10] D. Van Dyck, H. Lichte, K.D. vanderMast, Sub-angstrom structure characterisation: the brite-euram route towards one angstrom, Ultramicroscopy 64 (1996) 1–15.
[11] F.H. Li, H.F. Fan, Image deconvolution in high resolution electron microscopy by making use of sayre s equation, Acta Phys. Sin. Chin. 2 (1979) 276–278.
[12] H.F. Fan, Z.Y. Zhong, C.D. Zheng, F.H. Li, Image processing in high-resolution electron microscopy using the direct method. I, Phase Ext. Acta Cryst. A 41 (1985) 163–165.
[13] F.S. Han, H.F. Fan, F.H. Li, Image processing in high-resolution electron microscopy using the direct method. II. Image deconvolution, Acta Cryst. A 42 (1986) 353–356.
[14] J.J. Hu, F.H. Li, Maximum entropy image deconvolution in high resolution electron microscopy, Ultramicroscopy 35 (1991) 339–350.
[15] F.H. Li, Developing image-contrast theory and analysis methods in high-resolution electron microscopy, Phys. Status Solidi A 207 (2010) 2639–2665.
[16] R. Kilaas, L.D. Marks, C.S. Own, EDM 1.0: electron direct methods, Ultramicroscopy 102 (2005) 233–237.
[17] T. Willhammar, J. Sun, W. Wan, P. Oleynikov, D. Zhang, X. Zou, M. Moliner, J. Gonzalez, C. Martínez, F. Rey, A. Corma, Structure and catalytic properties of the most complex intergrown zeolite ITQ-39 determined by electron crystallography, Nat. Chem. 4 (2012) 188–194.
[18] W. Wan, S. Hovmöller, X. Zou, Structure projection reconstruction from through-focus series of high-resolution transmission electron microscopy images, Ultramicroscopy 115 (2012) 50–60.
[19] H. Rose, Outline of a spherically corrected semiaplanatic medium-voltage transmission electron microscope, Optik 85 (1990) 19–24.
[20] M. Haider, H. Rose, S. Uhlemann, B. Kabius, K. Urban, Towards 0.1 nm resolution with the first spherically corrected transmission electron microscope, J. Electron Microsc. 47 (1998) 395–405.
[21] M. Haider, H. Rose, S. Uhlemann, E. Schwan, B. Kabius, K. Urban, A spherical-aberration-corrected 200 kV transmission electron microscope, Ultramicroscopy 75 (1998) 53–60.
[22] M. Haider, S. Uhlemann, E. Schwan, H. Rose, B. Kabius, K. Urban, Electron microscopy image enhanced, Nature 392 (1998) 768–769.
[23] C.L. Jia, M. Lentzen, K. Urban, Atomic-resolution imaging of oxygen in perovskite ceramics, Science 299 (2003) 870–873.
[24] J.H. Chen, H.W. Zandbergen, D.V. Dyck, Atomic imaging in aberration-corrected high-resolution transmission electron microscopy, Ultramicroscopy 98 (2004) 81–97.
[25] C. Tang, J. Chen, H. Zandbergen, F. Li, Image deconvolution in spherical aberration-corrected high-resolution transmission electron microscopy, Ultramicroscopy 106 (2006) 539–546.
[26] M. Texier, J. Thibault-Pénisson, Optimum correction conditions for aberration-corrected HRTEM SiC dumbbells chemical imaging, Micron 43 (2012) 516–523.
[27] C. Wen, W. Wan, F.H. Li, D. Tang, Restoring defect structures in 3C–SiC/Si (0001) from spherical aberration-corrected high-resolution transmission electron microscope images by means of deconvolution processing, Micron 71 (2015) 22–31.
[28] Z.Q. Fu, D.X. Huang, F.H. Li, J.Q. Li, Z.X. Zhao, T.Z. Cheng, H.F. Fan, Incommensurate modulation in minute crystals revealed by combining high-resolution electron microscopy and electron diffraction, Ultramicroscopy 54 (1994) 229–236.
[29] J. Liu, F.H. Li, Z.H. Wan, H.F. Fan, X.J. Wu, T. Tamura, K. Tanabe, Incommensurate modulated structure of "Pb"-1223 determined by combining high resolution electron microscopy and electron diffraction, Mater. Trans. JIM 39 (1998) 920–926.
[30] C.-L. Jia, V. Nagarajan, J.-Q. He, L. Houben, T. Zhao, R. Ramesh, K. Urban, R. Waser, Unit-cell scale mapping of ferroelectricity and tetragonality in epitaxial ultrathin ferroelectric films, Nat. Mater. 6 (2006) 64–69.
[31] C.L. Jia, M. Lentzen, K. Urban, High-resolution transmission electron microscopy using negative spherical aberration, Microsc. Microanal. 10 (2004) 174–184.
[32] C.L. Jia, K. Urban, Atomic-resolution measurement of oxygen concentration in oxide materials, Science 303 (2004) 2001–2004.
[33] C.L. Jia, A. Thust, K. Urban, Atomic-scale analysis of the oxygen configuration at a $SrTiO_3$ dislocation core, Phys. Rev. Lett. 95 (2005).
[34] P.M. De Wolff, Pseudo-symmetry of modulated crystal-structures, Acta Cryst. A 30 (1974) 777–785.
[35] H. Luo, P. Cheng, L. Fang, H.-H. Wen, Growth and post-annealing studies of $Bi_2Sr_2-xLaxCuO_6+\delta (0 \le x \le 1.00)$ single crystals, Supercond. Sci. Technol. 21 (2008) 125024.

[36] Z.H. Wan, Y.D. Liu, Z.Q. Fu, Y. Li, T.Z. Cheng, F.H. Li, H.F. Fan, Visual computing in electron crystallography, ZKri 218 (2003) 308–315.
[37] X. Li, B. Ge, F. Li, H. Luo, H. Wen, A study of one-dimensional incommensurate modulated structure determination in high-resolution transmission electron microscopy, Acta Cryst. Sect. A 70 (2014) 563–571.
[38] C.C. Torardi, M.A. Subramanian, J.C. Calabrese, J. Gopalakrishnan, E. M. McCarron, K.J. Morrissey, T.R. Askew, R.B. Flippen, U. Chowdhry, A. W. Sleight, Structures of the superconducting oxides Tl_{2}Ba_{2}CuO_{6} and Bi_{2}Sr_{2}CuO_{6}, Phys. Rev. B 38 (1988) 225.
[39] F.H. Li, D. Tang, Pseudo-weak-phase-object approximation in high-resolution electron-microscopy. I. Theory, Acta Cryst. A 41 (1985) 376–382.
[40] M. Lentzen, Contrast transfer and resolution limits for sub-angstrom high-resolution transmission electron microscopy, Microsc. Microanal. 14 (2008) 16–26.
[41] R. Yu, M. Lentzen, J. Zhu, Effective object planes for aberration-corrected transmission electron microscopy, Ultramicroscopy 112 (2011) 15–21.
[42] S. Van Aert, A.J. den Dekker, D. Van Dyck, A. van den Bos, High-resolution electron microscopy and electron tomography: resolution versus precision, J. Struct. Biol. 138 (2002) 21–33.
[43] B. Ge, Y. Wang, Y. Chang, Y. Yao, Study of point spread in the aberration-corrected transmission electron microscopy, Microsc. Microanal. 20 (2014) 1447–1452.
[44] B.D. Sha, H.F. Fan, F.H. Li, Correction for the dynamical electron-diffraction effect in crystal-structure, Anal. Acta Cryst. A 49 (1993) 877–880.